



Robocasting of self-setting bioceramics: from paste formulation to 3D part characteristics

Ambra Paterlini, Sylvain Le Grill, Fabien Brouillet, Christèle Combes, David Grossin, Ghislaine Bertrand

► To cite this version:

Ambra Paterlini, Sylvain Le Grill, Fabien Brouillet, Christèle Combes, David Grossin, et al.. Robocasting of self-setting bioceramics: from paste formulation to 3D part characteristics. Open Ceramics, 2021, 5, pp.100070. 10.1016/j.oceram.2021.100070 . hal-03200389

HAL Id: hal-03200389

<https://hal.science/hal-03200389>

Submitted on 16 Apr 2021

HAL is a multi-disciplinary open access archive for the deposit and dissemination of scientific research documents, whether they are published or not. The documents may come from teaching and research institutions in France or abroad, or from public or private research centers.

L'archive ouverte pluridisciplinaire **HAL**, est destinée au dépôt et à la diffusion de documents scientifiques de niveau recherche, publiés ou non, émanant des établissements d'enseignement et de recherche français ou étrangers, des laboratoires publics ou privés.









Open Archive Toulouse Archive Ouverte (OATAO)

OATAO is an open access repository that collects the work of Toulouse researchers and makes it freely available over the web where possible

This is a Publisher's version published in: <http://oatao.univ-toulouse.fr/27604>

Official URL: <https://doi.org/10.1016/j.oceram.2021.100070>

To cite this version:

Paterlini, Ambra^{} and Le Grill, Sylvain^{} and Brouillet, Fabien^{} and Combes, Christèle^{} and Grossin, David^{} and Bertrand, Ghislaine^{}
Robocasting of self-setting bioceramics: from paste formulation to 3D part characteristics. (2021) Open Ceramics, 5. 100070. ISSN 2666-5395

Any correspondence concerning this service should be sent
to the repository administrator: tech-oatao@listes-diff.inp-toulouse.fr



Robocasting of self-setting bioceramics: from paste formulation to 3D part characteristics

A. Paterlini^{a,*}, S. Le Grill^{a,b}, F. Brouillet^b, C. Combes^a, D. Grossin^a, G. Bertrand^a

^a CIRIMAT, Université de Toulouse, CNRS, INP- ENSIACET, 4 Allée Emile Monso, BP44362, 31030, Toulouse, Cedex 4, France

^b CIRIMAT, Université de Toulouse, CNRS, Faculté des Sciences Pharmaceutiques, 35 Chemin des Maraichers, 31062, Toulouse, Cedex 4, France

ARTICLE INFO

Keywords:

Robocasting
Self-setting ceramic
Scaffolds
Calcium sulphate
Apatite

ABSTRACT

This study aims to investigate the feasibility of generating three-dimensional scaffold structures by robocasting 3D printing for bone tissue engineering and anatomical model applications. Robocasting is an additive manufacturing process that generates parts directly from CAD draws in a layer-wise manner, enabling the construction of complex 3D structures with controlled chemistry and specific interconnected porosity. Our strategy was based on the reactivity of the involved components in mineral bone cement or plaster self-setting pastes, but the simultaneity of manufacturing process and chemical setting reactions required a careful adaptation of paste formulations to secure enough time to fabricate a 3D scaffold under homogeneous extruding conditions at room temperature. The two self-setting pastes reactions studied in the present work were the transformation of calcium sulphate hemi-hydrate into gypsum and a mixture of brushite and vaterite into apatite. Additives such as carboxymethyl cellulose (CMC) or polyvinyl alcohol (PVA) were introduced in limited amounts (2–3% for CMC and 9–13% for PVA) in the self-setting paste formulations to favour extrusion while achieving self-standing brands. To complete the 3D scaffold setting reaction, a post-drying protocol was developed. 3D parts of various sizes and architectures were produced. Their crystalline phase and chemical composition characterisations allowed establishing the progress of the chemical setting reaction for all the pastes. A rheological study allowed defining a common trend for all the extruded pastes. Compression tests presented great mechanical properties of plaster 3D samples, particularly improved by the presence of PVA, while water absorption study presented suitable values for all the compositions, according to their different applications.

1. Introduction

During last decades, additive manufacturing (AM) of ceramics has emerged as a flexible and powerful technique for advanced manufacturing in the biomedical field. AM involves the direct or indirect production of three-dimensional (3D) parts from computer-aided design (CAD) drawings without the help of moulds, dies or other tools [1]. These technologies have been investigated in the orthopaedic, maxillofacial and dental fields for the production of surgical and diagnostic aids, prosthetic implants, drug delivery devices, and bone scaffolds [1–3]. Robocasting technique, defined as the method by which a paste-like material is deposited layer-by-layer through a nozzle to form a 3D part, is particularly widespread due to the low costs of devices and raw materials [4,5]. Furthermore, in case of ceramics AM, robocasting exhibits several additional advantages, among which variability of the materials to print is the major one compared to other AM technologies

requirements (i.e. narrow particle size distribution, excellent flowability, specific light absorption, and others according to the technology) [4,6,7]. Due to its adaptability and low cost, robocasting of ceramics is advancing fast in the biomedical field, especially for bone substitution and repair [8, 9].

In bone tissue engineering, the production of 3D parts to replace, improve or regenerate a damaged tissue is still challenging. Bone scaffolds should accomplish different requirements as biocompatibility, rapid production, fitting to irregular shape sites in the wound, adjusted mechanical properties for the corresponding bone defect and appropriate macroporosity to enable new bone formation and survival [10,11]. Robocasting technology allows to accomplish most of these requirements, in particular the manufacturing of irregular and porous shapes, but the global production process is still a bottleneck: for most case studies, the heat treatment required for samples debinding and sintering is challenging and time-consuming (up to few days) and the

* Corresponding author.

E-mail address: ambra.paterlini@lincotek.com (A. Paterlini).

<https://doi.org/10.1016/j.oceram.2021.100070>

Received 30 December 2020; Accepted 1 February 2021

Available online 6 February 2021

2666-5395/© 2021 The Author(s). Published by Elsevier Ltd on behalf of European Ceramic Society. This is an open access article under the CC BY-NC-ND license

(<http://creativecommons.org/licenses/by-nc-nd/4.0/>).

high temperatures can generate undesired secondary phases that affect the mechanical performances - as tricalcium phosphate or tetracalcium phosphate in the case of calcium phosphate-based bioceramics and composites [12–14].

The production of 3D scaffolds is not only relevant for bone tissue repair but an extensive use of AM is also carried out for the fabrication of anatomical models. Rapid prototyping of physical models allows a better understanding of complex anatomic structures and bring several benefits to assist in diagnosis, surgical planning and prosthesis design [15–18]. Furthermore, analyses of 3D printed models as a patient educational tool [19] or to improve the teaching of applied clinical anatomy [20] were carried out. In this case the main requirements are low cost and availability of raw materials, easy reproduction of complex shapes and good representativity of the anatomical mechanical response [21–23]. The current trend in the field is to use PLA (Polylactic Acid) fused filament; this polymer, however, presents very different mechanical behaviour comparing to bone structures [23].

This paper investigated the opportunity to combine the principle of self-setting applied to bioactive ceramics and robocasting as a 3D printing method. The selected materials were calcium phosphate cements for the production of bone-like apatite scaffolds and hydrated calcium sulphate for low-cost anatomical models. The self-setting reaction of pastes allows to significantly reduce the global manufacturing time, thanks to the omission of highly time-consuming debinding and sintering steps. Apatite cements were obtained from the chemical setting reaction of brushite and vaterite mixture with water. In literature these cements have been presented as a promising resorbable material for bone substitution [24]. Calcium sulphate dihydrate (gypsum, $\text{CaSO}_4 \cdot 2\text{H}_2\text{O}$) was obtained from the self-setting reactions of a hemi-hydrated calcium sulphate (Bassanite, $\text{CaSO}_4 \cdot \frac{1}{2}\text{H}_2\text{O}$) with water. This material was chosen because of its wide availability and low cost, as well as potential mechanical behaviour similar to bone, it also presents a long history in medical applications [25–27]. Additives such as carboxymethyl cellulose (CMC) or polyvinyl alcohol (PVA), selected for their biocompatibility [28,29], were introduced in limited amount in the paste formulations to improve the filament extrusion, as well as the 3D part structure and cohesiveness. Especially for bone scaffold applications, good mechanical properties are required to provide structural support during bone growth and remodelling [30], knowing that the compressive strength of human trabecular bone covers the range 5–60 MPa [31]. The scaffold behaviour in liquid environment is also important to favour cell penetration and bone ingrowth [32,33]. Based on these considerations, 3D parts were produced, and their mechanical properties and water absorption characterised.

2. Materials and methods

2.1. Materials

The calcium sulphate hemi-hydrate ($\text{CaSO}_4 \cdot \frac{1}{2}\text{H}_2\text{O}$) used was a commercial easily available *plaster of Paris*, while brushite ($\text{CaHPO}_4 \cdot 2\text{H}_2\text{O}$) and vaterite (CaCO_3) powders were synthesised by double decomposition from cationic and anionic aqueous solutions according to protocols previously published by Jacquot et al. [29,34]. Commercial polymeric additives (carboxymethyl cellulose, CMC or polyvinyl alcohol, PVA) were introduced in the formulation. The CMC used is a 7H4XF-PH type “blanose®” (Ashland, Aqualon®) with a molecular weight of $700000 \text{ g mol}^{-1}$, PVA was provided by Sigma-Aldrich® and has a molecular weight of $13000\text{--}23000 \text{ g mol}^{-1}$.

2.2. Powders characterisation

Calcium sulphate hemi-hydrate, brushite and vaterite powders, as well as printed materials, were characterised by X-ray diffraction (XRD)

analysis, Fourier transform infrared (FTIR) spectroscopy and thermogravimetric analysis (TGA). To characterise crystalline phases, XRD analyses were carried out using an *INEL Equinox 1000* diffractometer with a Co anode ($K\alpha = 1.78897 \text{ \AA}$). Chemical bonds and functional groups were investigated through FTIR spectroscopy using a *Nicolet 5700 Thermo* spectrometer. Spectra were obtained in far-infrared region ($400\text{--}4000 \text{ cm}^{-1}$) in transmission mode with a 2 cm^{-1} resolution after sampling in KBr pellets. The sample pellets were prepared by mixing 1 mg of powder with 300 mg of KBr, compressed under a 700 N pressure for 30 s. Thermogravimetric analyses under air were carried out on amounts of powder (10–15 mg) subjected to a linear programming of temperature. The protocol used for calcium sulphate included a temperature ramp between 25 and $500 \text{ }^\circ\text{C}$ at $10 \text{ }^\circ\text{C min}^{-1}$ [35,36]. Brushite and vaterite thermal analyses were carried out respectively on the temperature range $25 \text{ }^\circ\text{C--}600 \text{ }^\circ\text{C}$ [37,38] and $25 \text{ }^\circ\text{C--}900 \text{ }^\circ\text{C}$ [39], both following a linear rate of $10 \text{ }^\circ\text{C min}^{-1}$. After each thermal cycle, samples were cooled according to the inertia of the device.

2.3. Paste formulations

The suspension compositions studied in this work are self-setting pastes of calcium sulphate or calcium phosphate and calcium carbonate. The chemical setting reactions of the paste involve the transformation of calcium sulphate hemi-hydrate to calcium sulphate dihydrate, commonly known as *gypsum*, or of a brushite and vaterite mixture into apatite. A polymeric additive (carboxymethyl cellulose, CMC or polyvinyl alcohol, PVA) has been introduced in limited amounts in the formulations to improve paste extrusion and provide greater stability to the 3D printed object structure, without compromising paste homogeneity and injectability. The paste is produced by manually mixing, during about 2 min, the solid phase (S) and the liquid one (L) in a mortar: after the homogenisation of powders, the liquid phase is added according to the L/S mass ratio desired. Based on previous studies [29], for CMC-containing formulations L/S ratio was varied between 0.65 and 0.85 for plasters and between 1.0 and 1.6 for cements. In PVA-containing formulations, tested ratios covered the ranges 0.35–0.7 and 1.0–1.25 in case of plasters and cements, respectively. The compositions optimisation permitted to exclude higher L/S ratios because of the great paste fluency and lower values, which prevent to merge the components. CMC powders were introduced directly to the solid phase of the self-setting formulation whereas in the case of PVA-containing formulations PVA powders were previously dissolved in distilled water at $80 \text{ }^\circ\text{C}$ during 3 h and after cooling at ambient temperature this liquid phase was then added to the solid phase (brushite-vaterite or calcium sulphate).

2.4. Robocasting 3D printing

The printer was a BCN3D + model by BCN3D technologies (Barcelona, Spain) derived from RepRap open-source project. This device, planned for Fused Filament Fabrication (FFF) manufacturing technology, was revisited for robocasting. A syringe replaced the filament nozzle and a cogged plunger was fabricated to allow movements along z-axis (vertically on the support platform). A 100 mL syringe was used, with a 30 mm barrel diameter and a 1.5 mm nozzle. The support platform allows a printable volume of $252 \times 200 \times 200 \text{ mm}$; the processing software Slic3r, which supports STL files, operates the print process. During the formulation study, the printability of every composition was tested through the manufacturing of square prism and cylindrical geometries with 50 mm or 30 mm base sides and 5 mm high (corresponding to 5 or 6 layers). To overcome the printer limits in terms of extrusion force and syringe nozzle, some complementary tests were carried out using a texturometer (TA.XT Plus Texture Analyser model). Thanks to this device, it was possible to extrude finer paste filaments through a $504 \text{ }\mu\text{m}$ syringe nozzle.

2.5. Paste characterisation

2.5.1. Rheological behaviour of the pastes

A preliminary study of paste rheological behaviour was achieved using an AR 2000 rheometer by TA Instruments. To determine pseudo-viscosity, a stepped flow test was carried out using two different geometry combinations: cone–plate and striped parallel plates. The cone–plate geometry was used for plaster compositions, while the striped parallel plates were chosen for cement paste because of its slicker surface, probably due to a preferential orientation of the characteristic platelet-shape crystals of brushite [29]. Stepped flow test consists of a conditioning and a stepped flow stage. During the conditioning step, the temperature was set at 25 °C for 3 min (to reach thermal equilibrium). For the stepped flow stage, the shear rate range was varied between 0.01 and 600 s⁻¹, measuring 5 points per decade on a logarithmic scale. Data were viewed as stress and viscosity vs. shear rate. At least four samples were analysed for each paste formulation.

2.5.2. Drying treatments and setting reactions

Several drying treatments were tested by varying time, temperature and relative humidity. The setting time of the self-setting paste was evaluated by the Gillmore needle method (standard ISO 9917-1:2007). In addition, the total or partial occurrence of chemical setting reactions was verified with FTIR spectroscopy and XRD analyses under the same working conditions (paragraph 2.2).

2.6. 3D samples characterisation

Reference samples (without additives) were produced for comparison of 3D samples properties and thus evaluate the influence of polymers added to the formulations. The formulations used were L/S = 0.6 for plaster samples and L/S = 1.2 for cement ones. Samples shrinkage was evaluated by measuring filament diameter immediately after printing with a calibre and by comparing it with the final dimension after setting, using optical microscope image analysis by ImageJ software. SEM analysis were carried out with a FEI Quanta450 microscope, using low vacuum mode (90–110 Pa) and a high voltage of 10 kV.

2.6.1. Water absorption test

A water absorption test was carried out to evaluate the resistance of 3D printed cylindrical and prismatic samples in an aqueous environment. For every formulation eight specimens were tested, each one was initially weighed (± 0.0001 g) and then immersed in 10 mL of distilled water at 37 °C for 24 h (conditions chosen to approach human physiology). Successively, the samples were taken out, blotted on a dry filter paper to remove excess of water and weighed. The ratio of water absorption (W_a) was calculated according to the equation $W_a[\text{wt}\%] = 100n(w_f - w_0)/w_0$, where w_f and w_0 are the final and the initial weight of samples respectively [40,41].

2.6.2. Compression test

An MTS SYNERGIE 1000 device was employed to evaluate the compressive mechanical properties of 3D samples at room temperature. It must be noted that in this case the samples used were not 3D printed ones, due to the surface irregularity of the latter; thus, a silicone moulds shaping procedure of the plaster and cement pastes was preferred to obtain regular specimens and consequently to better assess the material mechanical properties. With this shaping process, the resulted specimens presented no visible macroporosity. These cylindrical specimens of 10 mm diameter and 20 mm high were placed between two steel plates and compressed with an imposed displacement of 0.02 mm s⁻¹ using a 5 kN load cell. A preload step was performed (100 N for calcium sulphate samples and 20 N for the apatite ones) in order to obtain a smooth surface on the scaffold and to limit the effect of surface irregularity due to fabrication process. The specimens were then unloaded down to 2 N compression; its height was then the initial value used to calculate the strain during the compression test carried out.

3. Results

3.1. Powders characterisation

The complementary characterisations of the raw powders proved their phase purity. The X-ray diffractograms shown in Fig. 1 present the various batches of synthesised and commercial powders. They were matched with JCPDS references 01-072-0713 for brushite, 01-072-0506 for vaterite and 01-081-1849 for calcium sulphate hemi-hydrate, respectively. Fig. 2 presents the powders FTIR spectra. The characteristic bands of calcium sulphate hemi-hydrate at 605 and 660 cm⁻¹ correspond to ν_4 vibrations of SO_4^{2-} ; a major and broad band appearing at 1000–1150 cm⁻¹ was assigned to the S–O stretching vibration of SO_4^{2-} group [42], as well as the sharp band at 1620 cm⁻¹; bands between 3650 and 3400 cm⁻¹ belong to O–H stretching vibration of water molecules [43]. Concerning brushite spectrum, bands at 3550–3165, 1650 and 660 cm⁻¹ all correspond to lattice water molecules, particularly to stretching, deformation and libration bands, respectively [44]. Bands between 960 and 1140 cm⁻¹ belong to P–O stretching mode, the 873 cm⁻¹ band refers to P–O(H) stretch and the 600–500 cm⁻¹ to P–O bending [45]. The vaterite main vibration bands were attributed according to Andersen et al. [46]: the vibration ν_3 of the carbonates was found between 1400 and 1500 cm⁻¹, ν_2 and ν_4 at 876 cm⁻¹ and 745 cm⁻¹, respectively. Bands corresponding to water molecule vibrations were found around 3420 cm⁻¹ [46]. Thermogravimetric properties of powders were analysed by measuring the sample mass loss during a specific heating cycle (Fig. 3). Calcium sulphate hemi-hydrate curve shows a 5% water loss between 80 °C and 200 °C, corresponding to the 0.5H₂O molecule of the component. For brushite two main zones were obtained: the first decomposition step between 100 °C and 350 °C was related to the loss of the two structural water molecules, consequently CaHPO₄ (monetite) was formed; the second one between 350 and 600 °C was attributed to the loss of 0.5 water molecule per Ca²⁺ ion and the formation of condensed calcium pyrophosphate (Ca₂P₂O₇), which is in good agreement with Betke et al. study [47]. Vaterite curve presents a first 2.5% mass loss below 200 °C, corresponding to the adsorbed water loss. At 400 °C, as confirmed by Donnay et al. analysis, there is a vaterite recrystallisation into calcite, which is finally decomposed between 600 °C and 750 °C by decarbonation [48].

3.2. Paste formulation and characterisation

Paste formulation was elaborated by varying two main parameters: the additive/reactive powders ratio and the L/S ratio. Table 1 shows the outcome of the formulation optimisation study, based on the injectability of the pastes by robocasting. As the chemical setting reactions of CaP cements and plaster of Paris are sensitive to temperature and presence of

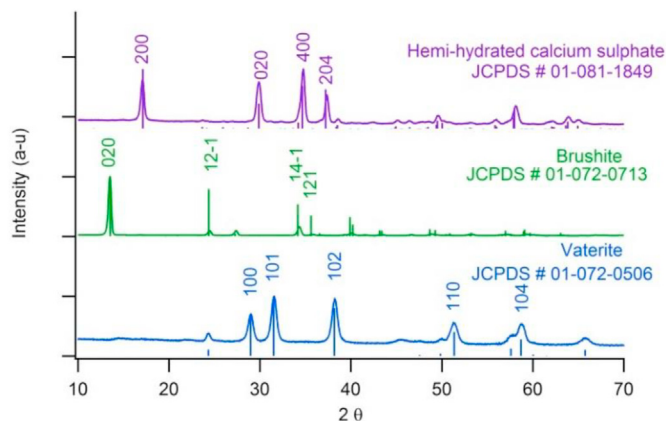


Fig. 1. XRD patterns of the reactive powders.

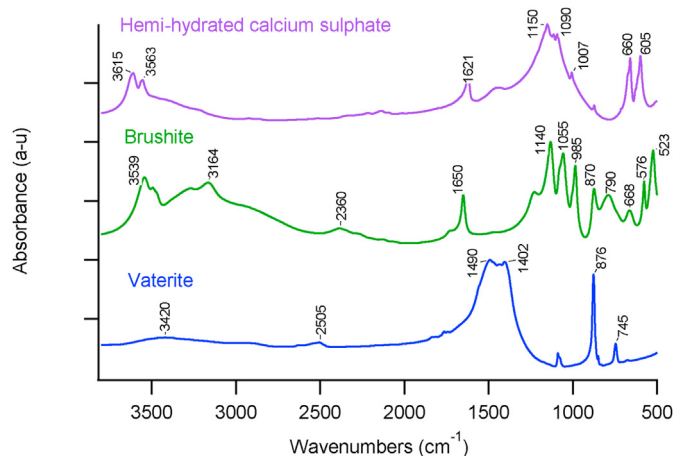


Fig. 2. FTIR spectra of the reactive powders.

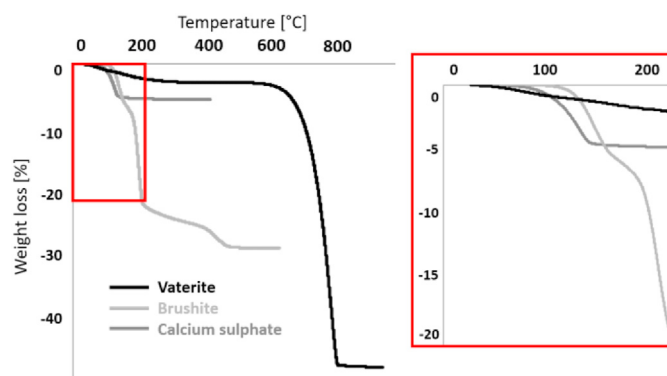


Fig. 3. TGA curves of the reactive powders; zoom on 0–200 °C range.

Table 1

The different paste formulations tested (weight ratios).

L: liquid phase (H ₂ O) S: solid phase		Materials	
		Hemi-hydrated calcium sulphate (HCS)	Brushite - Vaterite (B - V)
Additives	Polyvinyl alcohol (PVA)	L/S = 0.75 PVA/L = 0.13	L/S = 1.10 PVA/L = 0.13 B/S = V/S
	Carboxymethyl cellulose (CMC)	L/S = 0.75 CMC/S = 0.02 HCS/S = 0.98	L/S = 1.25 CMC/S = 0.03 B/S = V/S

water, during setting and hardening several drying/setting conditions were tested on the cement paste. A faster cement hardening and thus material cohesion was obtained when submitting samples to a water-saturated atmosphere at 37 °C during 3 h as a post-treatment. The occurrence of the chemical setting reaction was verified by XRD and FTIR spectroscopic analyses (Figs. 4 and 5).

XRD diffractograms of hardened cements show the transformation into apatite in the presence of each additive: the main peaks coincide with the hydroxyapatite lines of JCPDS reference (01-089-4405), although some amount of vaterite, initially introduced in excess, remained (particularly visible at 2θ values equal to 32, 38 and 51°). Calcium sulphate transformation into its dihydrate form was found in PVA-containing formulation, as shown by the corresponding X-ray diffractogram, matching with CaSO₄·2H₂O JCPDS reference (00-033-0311). Otherwise, no reaction occurred for CMC-containing formulations, the presence of CMC, which is a highly hydrophilic polysaccharide, limited the amount of water available to react with calcium sulphate hemi-

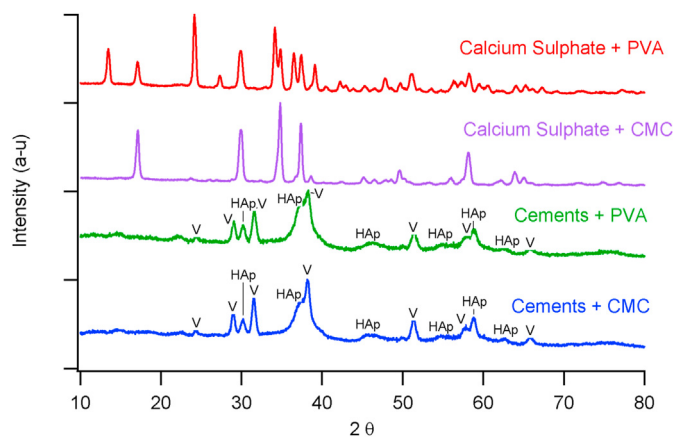


Fig. 4. XRD patterns of the materials (plaster and cement with or without additive) after hardening (HAp: nanocrystalline apatite; V: vaterite).

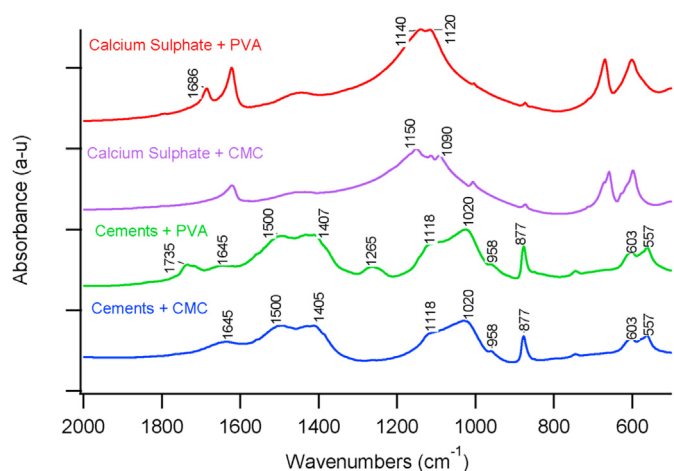


Fig. 5. FTIR spectra of the materials (plaster and cement with or without additive) after hardening.

hydrate powder and, despite their hardening and cohesiveness, samples were still constituted of the hemi-hydrated form of calcium sulphate (CaSO₄·0.5H₂O, JCPDS n°01-081-1849). The FTIR analysis (Fig. 5) confirmed this result. Indeed, the spectrum of PVA-containing calcium sulphate material was characteristic of the dihydrate form: the presence of 1686 cm⁻¹ band, typical of the H–O–H bending in calcium sulphate dihydrate (not found in the CMC formulation spectrum), confirmed it. Furthermore, S–O stretching vibration of SO₄²⁻ group are limited to the 1120–1140 cm⁻¹ zone for PVA spectrum, while they are extended between 1090 and 1150 cm⁻¹ for the CMC one, this difference is typical of dihydrate and hemi-hydrate phases respectively [49]. Concerning apatite cements, in both cases (PVA or CMC-containing formulations) the chemical setting reaction occurred. Carbonate characteristic bands assigned to ν₂ and ν₃ vibrations of CO₃²⁻ at 877 and 1405 cm⁻¹ [46] in vaterite were still visible and that of apatite (ν₃ vibrations of CO₃²⁻) were found at 1420–1500 cm⁻¹. In addition ν₄, ν₁, ν₃ vibrations of PO₄³⁻ of apatite at 603–557, 960 and 1020–1118 cm⁻¹ were also observed respectively [29]. PVA-containing cement composition also shows two characteristic PVA peaks at 1265 and 1735 cm⁻¹, assigned to C–O and C=O stretching [50].

3.2.1. Rheological analysis

Rheological analyses have produced very different results among the four self-setting paste formulations tested. In fact, the homogeneity and the long setting time of calcium sulphate paste allowed to complete the

test for almost all samples while concerning cement paste, the rapid hardening reaction prevented to obtain a coherent and significant measurements. For this reason, the results for cement composition were discarded from the study. Fig. 6 presents the evolution of paste viscosity and shear stress as a function of increasing shear rate for calcium sulphate compositions. The resulting curves followed Herschel-Bulkley model, which is represented by its characteristic equation: $\tau = \tau_0 + k\dot{\gamma}^n$, where τ is shear stress [Pa], τ_0 the threshold yield stress [Pa], $\dot{\gamma}$ the shear rate [s^{-1}], k is a consistency index which gives an idea of the fluid viscosity [Pa·s] and n is a flow behaviour index. When n is close to 1 the fluid's behaviour tends to pass from shear thinning to shear thickening, when it is above 1 the fluid acts as a shear thickening fluid [51]. The function trend line and the associated parameters, listed in Table 2, were obtained from mathematical treatment of the data using Origin software.

3.3. 3D materials characterisation

The characterisation of 3D samples was carried out onto all the compositions studied and the corresponding references, except for calcium sulphate with CMC because of the lack of chemical setting reaction. Samples structure are illustrated in Fig. 7, while SEM images in Fig. 8 present some details about the thinner filaments extruded by the texturometer. In the presence of PVA, a particular porosity is noticed, in the order of 20–50 μm ; CMC-containing cements, instead, present no visible pores but a more irregular surface, due to the unset brushite and vaterite particles. PVA-plaster composites result in a volume shrinkage of $7\% \pm 3\%$, this variation is higher for apatite cements: $15\% \pm 4\%$ for PVA formulations and $13\% \pm 5\%$ for CMC ones.

3.3.1. Water absorption test

Water absorption results are reported in Fig. 9. Calcium sulphate samples present low percentages of absorbed water: $36.6\% \pm 0.5\%$ for reference sample (without additive) and $19\% \pm 3\%$ for PVA formulation. On the contrary, apatite cement compositions exhibit very high values: $136\% \pm 2\%$, $53\% \pm 3\%$, $119.8\% \pm 0.6\%$ for reference, PVA and CMC formulations, respectively.

3.3.2. Compression test

Fig. 10 illustrates compression test results. Mean curves were calculated from the outcomes of 5 samples tested for each material composition. Maximal compressive strength presented higher values for calcium sulphate samples: 19 ± 1 MPa for PVA-containing formulations, 10 ± 2 MPa for the reference material (without additive). Four to five times lower values were observed for cements: 4.0 ± 0.5 MPa for PVA formulations, 2.6 ± 0.5 MPa for CMC ones and 2.4 ± 0.4 MPa for reference specimens. The mechanical behaviour of samples under compression loading was very similar for all the tested materials: rupture occurred after a slight swelling in the central part of the cylinder and the main cracks were vertically oriented (along the loading axis).

4. Discussion

Initial powders characterisation by FTIR spectroscopy, XRD and TG analyses demonstrated the purity of the synthesised and commercial products: these reference data are essential to check then if the chemical setting reaction occurred or not within the two studied self-setting 3D printed systems. For every injectable composition obtained after the formulation optimisation cycle, FTIR spectra and XRD diffractograms verified the chemical setting reactions, except for the CMC-containing plaster formulation. The high hydrophilicity and water absorption ability of the polysaccharide prevented the chemical transformation into calcium sulphate dihydrate even after a post-treatment in water-saturated atmosphere. Concerning the extruded pastes, the rheology analysis presented a shear thinning behaviour for all the formulations. Shear rate values ($\dot{\gamma}$) involved in the current 3D printing set – at the inner wall of the syringe – were calculated approximating the flow to a New-

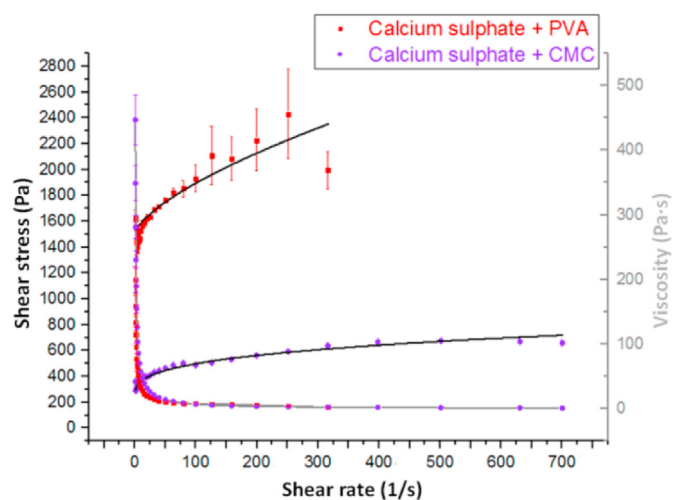


Fig. 6. Paste rheological curves - normal stress and viscosity vs. shear rate – of calcium sulphate formulations with CMC (violet) and with PVA (red). (For interpretation of the references to colour in this figure legend, the reader is referred to the Web version of this article.)

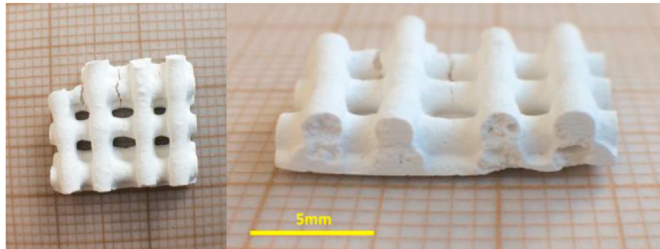
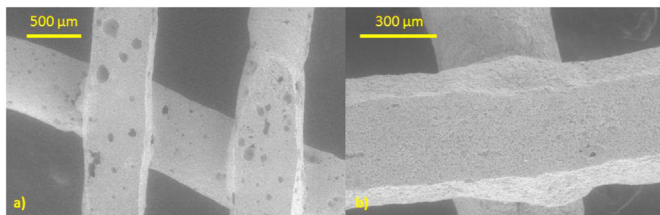
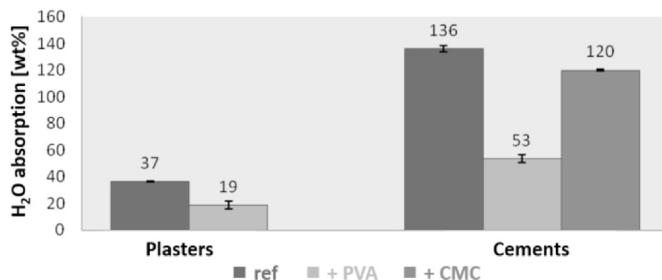
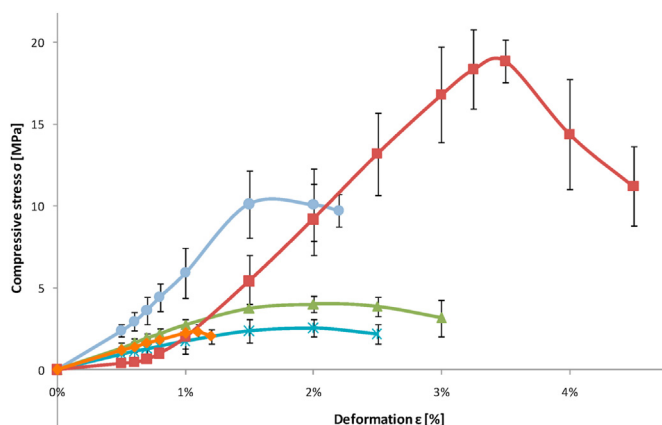
tonian fluid: $\dot{\gamma} = 4Q/\pi r^3$ [52]. Q represents the maximal paste flow rate of $2.25 \text{ mm}^3 \text{ s}^{-1}$ (obtained by multiplying maximal extrusion velocity, 0.01 mm s^{-1} , by syringe area, $225\pi \text{ mm}^2$) and r the exit nozzle radius of 0.75 mm , thus the shear rate has maximal values of around 20 s^{-1} . As shown in Fig. 6, the compositions presented comparable viscosity values in the order of 200 Pa s at these shear rates. The main differences due to the additive concerned the stress values: PVA-containing formulations curves presented about six times higher values of yield stress (σ_0) compared with CMC-containing ones, thus they required higher critical stress to launch the paste extrusion. However, the high variation of paste rheological properties due to air exposure drying must be considered: time for paste preparation and test set-up can significantly influence paste conditions (hydration state) due to high surface area exposed to air and to the rapid hardening development in these self-setting systems. Several studies in literature already demonstrated that Herschel-Bulkley fluid is a suitable model for extrudable pastes [53–55]. An ideal printable composition need high yield stress (σ_0) to assure that the lower layers of a piece can support the weight of the layers above them, the printed filament maintains its shape after the extrusion and to prevent pouring phenomena at the syringe nozzle [55]. Furthermore, a low n value indicating strong shear thinning and a low viscosity parameter (K) facilitate the extrusion process. Thus, as illustrated in Table 2, calcium sulphate and PVA formulation provided the most suited results in terms of rheology.

Also, 3D samples characterisation highlighted some variations among the four formulations. Concerning water absorption test, the influence of PVA filmogenic properties was noticed: PVA-containing formulations presented lower mass percentages absorbed - in the order of 50% - compare to CMC-containing formulations and reference materials, which showed absorption values over 100%. The ability of a scaffold to retain water is an important index to evaluate its efficacy for bone tissue engineering, it has been reported that water uptake capability of a composite material can significantly affect cell proliferation for bone regeneration [56–58]. According to literature, values in the order of 100% are suitable for this kind of scaffolds [33,40,57]. In terms of mechanical properties, PVA-containing samples manifested advantageous results. Strength values obtained through compression test were largely higher in the case of calcium sulphate and PVA composite material, which presented a maximal strength of around 20 MPa, twice as high as the reference sample one. Cement samples, instead, exhibited significantly lower values, in the order of 2.5 for CMC-containing composite materials to 4 MPa for PVA-containing ones.

Table 2

Herschel-Bulkley model parameters obtained from rheological data of the studied plaster formulations.

formulation	τ_0	k	n	R^2
Calcium sulphate + CMC	227 ± 23	66 ± 17	0.31 ± 0.04	0.99
Calcium sulphate + PVA	1498 ± 34	19 ± 11	0.66 ± 0.11	0.84

**Fig. 7.** 3D printed parts of plaster samples.**Fig. 8.** Filament details by SEM a) cement + PVA, b) cement + CMC.**Fig. 9.** Water absorption percentage for the different 3D materials prepared.**Fig. 10.** Compressive stress curves of reference plaster (●), plaster + PVA (■), reference cement (◆), cement + PVA (▲) and cement + CMC (×).

5. Conclusions

According to the characterisation of tested pastes, self-setting occurrence was verified for all the formulations except for the calcium sulphate hemi-hydrate in presence of CMC. Both the analysed compositions presented a suitable rheological behaviour for 3D printing, particularly calcium sulphate and PVA paste formulations. Concerning 3D samples, calcium phosphate cement compositions showed favourable values of water retention, although they were halved in presence of PVA. On the other hand, calcium sulphate and PVA specimens had largely lower absorption rates; these properties would be more adapted to their applications for anatomical models. Furthermore, calcium sulphate and PVA composite material presented good mechanical properties, with comparable values to the cancellous bone ones. All of these results indicate that calcium sulphate artificial scaffolds are suitable for bone models, while calcium phosphate cements may require an investigation on alternative additives to get an additional amelioration of mechanical properties and a different extrusion nozzle to improve the resolution (texturometer tests demonstrated the pastes extrudability by thinner faucets). Nevertheless, the printability of pastes was demonstrated for both case studies and their use as biocompatible and bioactive materials and anatomic models is increasingly interesting because of the self-setting properties, freeform design and cost-effectiveness.

This research did not receive any specific grant from funding agencies in the public, commercial, or not-for-profit sectors.

Declaration of competing interest

The authors declare that they have no known competing financial interests or personal relationships that could have appeared to influence the work reported in this paper.

References

- [1] Q. Hou, P.A. De Bank, K.M. Shakesheff, Injectable scaffolds for tissue regeneration, *J. Mater. Chem.* 14 (2004) 1915–1923, <https://doi.org/10.1039/b401791a>.
- [2] I. Gibson, D.W. Rosen, B. Stucker, *Additive Manufacturing Technologies*, Springer, US, 2010, <https://doi.org/10.1007/978-1-4419-1120-9>.
- [3] Y.W. Moon, I.J. Choi, Y.H. Koh, H.E. Kim, Porous alumina ceramic scaffolds with biomimetic macro/micro-porous structure using three-dimensional (3-D) ceramic/camphene-based extrusion, *Ceram. Int.* 41 (2015) 12371–12377, <https://doi.org/10.1016/j.ceramint.2015.06.069>.
- [4] A. Zocca, P. Colombo, C.M. Gomes, J. Günster, Additive manufacturing of ceramics: issues, potentialities, and opportunities, *J. Am. Ceram. Soc.* 98 (2015) 1983–2001, <https://doi.org/10.1111/jace.13700>.
- [5] J. Deckers, J. Vleugels, J.P. Kruth, Additive manufacturing of ceramics: a review, *J. Ceram. Sci. Technol.* 5 (2014) 245–260, <https://doi.org/10.4416/JCST2014-00032>.
- [6] Z. Chen, Z. Li, J. Li, C. Liu, C. Lao, Y. Fu, C. Liu, Y. Li, P. Wang, Y. He, 3D printing of ceramics: a review, *J. Eur. Ceram. Soc.* 39 (2019) 661–687, <https://doi.org/10.1016/j.jeurceramsoc.2018.11.013>.
- [7] E. Feilden, E.G.T. Blanca, F. Giuliani, E. Saiz, L. Vandeperre, Robocasting of structural ceramic parts with hydrogel inks, *J. Eur. Ceram. Soc.* 36 (2016) 2525–2533, <https://doi.org/10.1016/j.jeurceramsoc.2016.03.001>.
- [8] E. Peng, D. Zhang, J. Ding, Ceramic robocasting: recent achievements, potential, and future developments, *Adv. Mater.* 30 (2018) 1–14, <https://doi.org/10.1002/adma.201802404>.
- [9] E. Feilden, C. Ferraro, Q. Zhang, E. García-Tuñón, E. D'Elia, F. Giuliani, L. Vandeperre, E. Saiz, 3D printing bioinspired ceramic composites, *Sci. Rep.* 7 (2017) 1–9, <https://doi.org/10.1038/s41598-017-14236-9>.
- [10] K.J.L. Burg, S. Porter, J.F. Kellam, Biomaterial developments for bone tissue engineering, *Biomaterials* 21 (2000) 2347–2359.

- [11] S. Bose, S. Vahabzadeh, A. Bandyopadhyay, Bone tissue engineering using 3D printing, *Mater. Today* 16 (2013) 496–504, <https://doi.org/10.1016/j.mattod.2013.11.017>.
- [12] I. Mobasherpour, M. Solati Hashjin, S.S. Razavi Toosi, R. Darvishi Kamachali, Effect of the addition ZrO₂-Al₂O₃ on nanocrystalline hydroxyapatite bending strength and fracture toughness, *Ceram. Int.* 35 (2009) 1569–1574, <https://doi.org/10.1016/j.ceramint.2008.08.017>.
- [13] M. Hounard, Q. Fu, M. Genet, E. Saiz, A.P. Tomsia, On the structural, mechanical, and biodegradation properties of HA/ β -TCP robocast scaffolds, *J. Biomed. Mater. Res. B Appl. Biomater.* 101 (2013) 1233–1242, <https://doi.org/10.1002/jbm.b.32935>.
- [14] M. Aminzare, A. Eskandari, M.H. Baroonian, A. Berenov, Z. Razavi Hesabi, M. Taheri, S.K. Sadrnezhad, Hydroxyapatite nanocomposites: synthesis, sintering and mechanical properties, *Ceram. Int.* 39 (2013) 2197–2206, <https://doi.org/10.1016/j.ceramint.2012.09.023>.
- [15] S.J. Esses, P. Berman, A.I. Bloom, J. Sosna, Clinical applications of physical 3D models derived from MDCT data and created by rapid prototyping, *Am. J. Roentgenol.* 196 (2011) 683–688, <https://doi.org/10.2214/AJR.10.5681>.
- [16] M.D.B.S. Tam, S.D. Laycock, J.R.I. Brown, M. Jakeways, 3D printing of an aortic aneurysm to facilitate decision making and device selection for endovascular aneurysm repair in complex neck anatomy, *J. Endovasc. Ther.* 20 (2013) 863–867.
- [17] M.W. Itagaki, Using 3D printed models for planning and guidance during endovascular intervention: a technical advance, *Diagnostic Interv. Radiol.* 21 (2015) 338–341, <https://doi.org/10.5152/dir.2015.14469>.
- [18] C.F. Smith, N. Tollemache, D. Covill, M. Johnston, Take away body parts! an investigation into the use of 3D-printed anatomical models in undergraduate anatomy education, *Anat. Sci. Educ.* 11 (2018) 44–53, <https://doi.org/10.1002/ase.1718>.
- [19] F. Rengier, A. Mehndiratta, H. Von Tengg-kobligk, C.M. Unterhinninghofen, R. Zechmann, F.L. Giesel, 3D printing based on imaging data: review of medical applications, *Int. J. Comput. Assist. Radiol. Surg.* 5 (2010) 335–341, <https://doi.org/10.1007/s11548-010-0476-x>.
- [20] P.G. Mcmenamin, M.R. Quayle, C.R. Mchenry, J.W. Adams, The production of anatomical teaching resources using three-dimensional (3D) printing technology, *Anat. Sci. Educ.* 7 (2014) 479–486, <https://doi.org/10.1002/ase.1475>.
- [21] T.M. Bücking, E.R. Hill, J.L. Robertson, E. Maneas, A.A. Plumb, D.I. Nikitichev, From medical imaging data to 3D printed anatomical models, *PloS One* 12 (2017) 1–10, <https://doi.org/10.1371/journal.pone.0178540>.
- [22] L. Brouwers, A. Teutelink, F.A.J.B. van Tilborg, M.A.C. de Jongh, K.W.W. Lansink, M. Bemelman, Validation study of 3D-printed anatomical models using 2 PLA printers for preoperative planning in trauma surgery, a human cadaver study, *Eur. J. Trauma Emerg. Surg.* 45 (2019) 1013–1020, <https://doi.org/10.1007/s00068-018-0970-3>.
- [23] N. Nagarajan, A. Dupret-Bories, E. Karabulut, P. Zorlutuna, N.E. Vrana, Enabling personalized implant and controllable biosystem development through 3D printing, *Biotechnol. Adv.* 36 (2018) 521–533, <https://doi.org/10.1016/j.biotechadv.2018.02.004>.
- [24] C. Combes, R. Bareille, C. Rey, Calcium carbonate-calcium phosphate mixed cement compositions for bone reconstruction, *J. Biomed. Mater. Res.* 79 (2006) 318–328.
- [25] Y.K. Modi, Calcium sulphate-based 3D printed tooling for vacuum forming of medical devices: an experimental evaluation, *Mater. Technol.* 33 (2018) 642–650, <https://doi.org/10.1080/10667857.2018.1491933>.
- [26] B.D. Boyan, M.I. Baker, C.S.D. Lee, A.L. Raines, A.S. Greenwald, R. Olivares-Navarrete, Z. Schwartz, Bone tissue grafting and tissue engineering concepts, in: *Orthop. Surg. – Fract. Fixat. Bone Grafting, Tendon Ligament Repair*, Elsevier Ltd, 2011, pp. 237–255, <https://doi.org/10.1016/b978-0-12-803581-8.10240-1>.
- [27] Z. Zhou, C.A. Mitchell, F.J. Buchanan, N.J. Dunne, Effects of heat treatment on the mechanical and degradation properties of 3D-printed calcium-sulphate-based scaffolds, *ISRN Biomater* (2013) 1–10, <https://doi.org/10.5402/2013/750720>.
- [28] G. Wu, B. Su, W. Zhang, C. Wang, In vitro behaviours of hydroxyapatite reinforced polyvinyl alcohol hydrogel composite, *Mater. Chem. Phys.* 107 (2008) 364–369, <https://doi.org/10.1016/j.matchemphys.2007.07.028>.
- [29] S. Jacquart, *Substitut osseux injectable, antibactérien et résorbable : études physico-chimiques et biologiques d'un ciment composite à base d'apatite*, PhD Thesis, Institut National Polytechnique de Toulouse, 2013.
- [30] C. Chang, C. Lin, F. Liu, M.H. Chen, C. Lin, 3D printing bioceramic porous scaffolds with good mechanical property and cell affinity, *PloS One* 10 (2015) 1–15, <https://doi.org/10.1371/journal.pone.0143713>.
- [31] S.A. Goldstein, The mechanical properties of trabecular bone: dependence on anatomic location and function, *J. Biomech.* 20 (1987) 1055–1061.
- [32] Z. Li, H.R. Ramay, K.D. Hauch, D. Xiao, M. Zhang, Chitosan – alginate hybrid scaffolds for bone tissue engineering, *Biomaterials* 26 (2005) 3919–3928, <https://doi.org/10.1016/j.biomaterials.2004.09.062>.
- [33] W.W. Thein-Han, R.D.K. Misra, Biomimetic chitosan–nanohydroxyapatite composite scaffolds for bone tissue engineering, *Acta Biomater.* 5 (2009) 1182–1197, <https://doi.org/10.1016/j.actbio.2008.11.025>.
- [34] S. Jacquart, R. Siadous, C. Henocq-pigasse, R. Bareille, C. Roques, C. Rey, Composition and properties of silver-containing calcium carbonate – calcium phosphate bone cement, *J. Mater. Sci. Mater. Med.* 24 (2015) 2665–2675, <https://doi.org/10.1007/s10856-013-5014-2>.
- [35] Z. Miao, H. Yang, Y. Wu, H. Zhang, X. Zhang, Experimental studies on decomposing properties of desulfurization gypsum in a thermogravimetric analyzer and multi-atmosphere fluidized beds, *Ind. Eng. Chem. Res.* 51 (2012) 5419–5423.
- [36] L. Pel, H.P. Huinink, K. Kopinga, Moisture transport and dehydration in heated gypsum, an NMR study, *Chem. Eng. Sci.* 66 (2011) 4241–4250, <https://doi.org/10.1016/j.ces.2011.06.024>.
- [37] A. Dosen, Thermal decomposition of brushite, CaHPO₄·2H₂O to monetite CaHPO₄ and the formation of an amorphous phase, *Am. Mineral.* 96 (2011) 368–373, <https://doi.org/10.2138/am.2011.3544>.
- [38] D. Ren, Q. Ruan, J. Tao, J. Lo, S. Nutt, J. Moradian-oldak, Amelogenin affects brushite crystal morphology and promotes its phase transformation to monetite, *Cryst. Growth Des.* 16 (2016) 4981–4990, <https://doi.org/10.1021/acs.cgd.6b00569>.
- [39] M. Maciejewski, H.R. Oswald, A. Reller, Thermal transformations of vaterite and calcite, *Thermochim. Acta* 234 (1994) 315–328, [https://doi.org/10.1016/0040-6031\(94\)85155-7](https://doi.org/10.1016/0040-6031(94)85155-7).
- [40] C.R. Kothapalli, M.T. Shaw, M. Wei, Biodegradable HA-PLA 3-D porous scaffolds: effect of nano-sized filler content on scaffold properties, *Acta Biomater.* 1 (2005) 653–662, <https://doi.org/10.1016/j.actbio.2005.06.005>.
- [41] S. Deb, M. Braden, W. Bonfield, Water absorption characteristics of modified hydroxyapatite bone cements, *Biomaterials* 16 (1995) 1095–1100.
- [42] A. Pundir, M. Garg, R. Singh, Evaluation of properties of gypsum plaster-superplasticizer blends of improved performance, *J. Build. Eng.* 4 (2015) 223–230, <https://doi.org/10.1016/j.jobbe.2015.09.012>.
- [43] H. Morillas, P. Vasco, E. Herriko, P. Colombar, M. Curie, The role of marine aerosol in the formation of (double) sulphate/nitrate salts in plasters, *Microchem. J.* 123 (2015) 148–157, <https://doi.org/10.1016/j.microc.2015.06.004>.
- [44] L. Tortet, J.R. Gavarrí, G. Nihoul, Study of protonic mobility in CaHPO₄·2H₂O (brushite) and CaHPO₄ (monetite) by infrared spectroscopy and neutron scattering, *J. Solid State Chem.* 132 (1997) 6–16.
- [45] I. Petrov, B. Soptrajanov, N. Fuson, Infra-red investigation of dicalcium phosphates, *Spectrochim. Acta* 23 (1967) 2637–2646.
- [46] A. Andersen, L. Brecevic, Infrared spectra of amorphous and crystalline calcium carbonate, *Acta Chem. Scand.* 45 (1991) 1018–1024.
- [47] A. Betke, G. Kickelbick, Bottom-up, wet chemical technique for the continuous synthesis of inorganic nanoparticles, *INORGA 2* (2014) 1–15, <https://doi.org/10.3390/inorganics2010001>.
- [48] J.D.H. Donnay, Optical determination of water content in spherulitic vaterite, *Acta Crystallogr.* 22 (1967) 312–314, <https://doi.org/10.1107/S0365110X67000532>.
- [49] R.J. Morris, Infrared spectrophotometric analysis of calcium sulphate hydrates using internally standardized mineral oil mulls, *Anal. Chem.* 35 (1963) 1489–1492.
- [50] J. Yang, J. Park, D. Kim, D. Lee, Effects of calcium carbonate as the expanding inhibitor on the structural and mechanical properties of expanded starch/polyvinyl alcohol blends, *J. Appl. Polym. Sci.* 93 (2004) 1762–1768, <https://doi.org/10.1002/app.20625>.
- [51] A. Björn, P. Segura De, L. Monja, A. Karlsson, J. Ejlerstsson, B.H. Svensson, Rheological Characterization, *Biogas*, 2012, <https://doi.org/10.5772/32596>.
- [52] Y. Son, Determination of shear viscosity and shear rate from pressure drop and flow rate relationship in a rectangular channel, *Sci. Direct.* 48 (2007) 632–637, <https://doi.org/10.1016/j.polymer.2006.11.048>.
- [53] Y. Shao, D. Chaussy, P. Grosseau, D. Beneventi, Use of microfibrillated cellulose/lignosulfonate blends as carbon precursors: impact of hydrogel rheology on 3D printing, *Ind. Eng. Chem. Res.* 54 (2015) 10575–10582, <https://doi.org/10.1021/acs.iecr.5b02763>.
- [54] J.O. Hardin, T.J. Ober, A.D. Valentine, J.A. Lewis, Microfluidic printheads for multimaterial 3D printing of viscoelastic inks, *Adv. Mater.* 27 (2015) 3279–3284, <https://doi.org/10.1002/adma.201500222>.
- [55] E. Feilden, E.G.T. Blanca, F. Giuliani, E. Saiz, L. Vandeperre, Robocasting of structural ceramic parts with hydrogel inks, *J. Eur. Ceram. Soc.* 36 (2016) 2525–2533, <https://doi.org/10.1016/j.jeurceramsoc.2016.03.001>.
- [56] A. Sionkowska, J. Kozłowska, Properties and modification of porous 3-D collagen/hydroxyapatite composites, *Int. J. Biol. Macromol.* 52 (2013) 250–259, <https://doi.org/10.1016/j.ijbiomac.2012.10.002>.
- [57] A. Shavandi, A.E.D.A. Bekhit, M.A. Ali, Z. Sun, Bio-mimetic composite scaffold from mussel shells, squid pen and crab chitosan for bone tissue engineering, *Int. J. Biol. Macromol.* 80 (2015) 445–454, <https://doi.org/10.1016/j.ijbiomac.2015.07.012>.
- [58] A. Moatary, A. Teimouri, M. Bagherzadeh, A.N. Chermahini, R. Razavizadeh, Design and fabrication of novel chitin hydrogel/chitosan/nano diopside composite scaffolds for tissue engineering, *Ceram. Int.* 43 (2017) 1657–1668, <https://doi.org/10.1016/j.ceramint.2016.06.068>.